Gold nanoparticles decorated rGO-ZnCo$_2$O$_4$ nanocomposite: A promising positive electrode for high performance hybrid supercapacitors

Swati J. Patil[a], Deepak P. Dubal[b], Dong-Weon Lee[a,c,*]

[a] MEMS and Nanotechnology Laboratory, School of Mechanical Engineering, Chonnam National University, Gwangju 61186, Republic of Korea
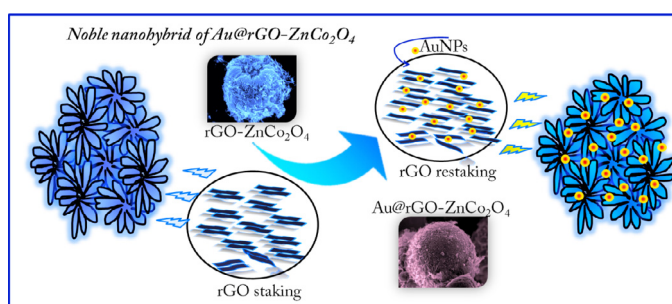[b] School of Chemistry, Physics and Mechanical Engineering, Queensland University of Technology (QUT), 2 George Street, Brisbane, QLD 4001, Australia
[c] Center for Next-generation Sensor Research and Development, Chonnam National University, Gwangju 61186, Republic of Korea

HIGHLIGHTS

- AuNPs decorated rGO-ZnCo$_2$O$_4$ nanohybrid prepared by a hydrothermal process.
- Au@rGO-ZnCo$_2$O$_4$ cauliflower electrode shows a specific capacity of 288.5 mAh g^{-1}.
- Au@rGO-ZnCo$_2$O$_4$//AC hybrid cell delivered a power density of 2121 W kg^{-1}.
- Fabricated hybrid supercapacitor retained about 97.1% capacity over 5000 cycles.

GRAPHICAL ABSTRACT

ARTICLE INFO

ABSTRACT

Herein, we have engineered gold nanoparticles decorated reduced graphene oxide-ZnCo$_2$O$_4$ hybrid material by a hydrothermal process. With exercising benefit of a synergistic influence of reduced graphene oxide and gold nanoparticles, the nanohybrid ensures that internal microstructure is altered from ZnCo$_2$O$_4$ microflower to Au@rGO-ZnCo$_2$O$_4$ cauliflower. The prepared Au@rGO-ZnCo$_2$O$_4$ cauliflower electrode shows a high specific capacity of 288.5 mAh g^{-1} at 2 mV s^{-1} scan rate. The more detailed electrochemical interpretation is carried out to understand the charge storage abilities of the electrodes occurred from the capacitive- and diffusion-controlled kinetics processes. These excellent electrochemical performances can be assigned to the incorporation of gold nanoparticles and reduced graphene oxide nanosheets that alleviate electrons exchange and transmit through electrochemical active sites, which create an electronic and structural heterogeneity of the electro-active material. Further, Au@rGO-ZnCo$_2$O$_4$//AC hybrid solid-state supercapacitor cell is designed with polymeric gel electrolyte that delivered a good power density of 2121 W kg^{-1} at an energy density of 31 Wh kg^{-1} with excellent capacitance retention over 5000 cycles highlights convenience of the utility of mixing high capacity with high electronic transport. The experimental results reveal that the noble metal nanoparticles incorporated hybrid nanostructures are promising electrode materials for energy storage applications.

* Corresponding author at: MEMS and Nanotechnology Laboratory, School of Mechanical Engineering, Chonnam National University, Gwangju, 61186, Republic of Korea.
E-mail address: mems@jnu.ac.kr (D.-W. Lee).

1. Introduction

Rapid installation of multifunction devices and blossoming wearable technologies have made a new era of interest in our obvious lifestyle. Simultaneously requisite heightened demands of portable, lightweight and wearable units are growing necessary to fulfill the requirements related to innovative electrochemical energy storage and conversion technologies for various future applications. For instance, eco-friendly efficient electrochemical energy storage, such as batteries, supercapacitors, fuel cells, has seen significant progress and great capabilities while embedding in several related applications, e.g. wearable and portable electronics, electromobiles, and smart power grids [1–3]. Grievously, the sale of these electrical appliances has a high cost, low power strength, insufficient self-sufficiency, and so on. Hence, great efforts have been made to improve the practical applications of these compliant standards and an array of the encouraged nano-structure electrode material with tailored structure, reasonable surface morphologies and compositions needed [4].

Graphene is a most attractive version of carbon and has important features for accomplishing high-energy storage capacity and high power density in supercapacitors due to their high volume to surface area ratio and good conductivity [5]. The flexibility and comprehensive electrochemical properties of graphene have been widely investigated as energy storage materials [6]. Another aspect involving metal-based oxides/hydroxides/sulfides, conductive polymers, etc., allows for a fast faradic oxidation-reduction process on the electrode surface that contributes to large charge storage capacities with a significantly higher energy density than carbon-based materials [7–9]. Among which bimetallic oxides such as $CoMn_2O_4$, $NiCo_2O_4$, $NiFe_2O_4$, and $ZnCo_2O_4$ possess a close-packed cubic and tetragonal structure of oxygen atoms systems with a synergetic effect of a couple of cations. In such spinel systems, octahedral and tetrahedral voids are occupied by different valence cations. Amongst the $ZnCo_2O_4$ is a member of the spinel transition oxide family and characteristic cobaltate with Zn^{2+} ions occupying the tetrahedral sites of spinel Co_3O_4 [10]. The eco-friendly, inexpensive and abundant Zn, Co elements exhibit the high render electrochemical activities hence it is successfully employed in energy storage applications and oxygen reduction reaction electrocatalysts. Moreover, spinel transition metal oxides have been thoroughly studied in electrochemistry with various nanostructure architectures and their diverse chemical configurations leading to the low activation energy for electron transport between multiple cations [11–13]. However, metal oxides suffer from poor electrical conductivity, which limits their practical applicability.

An excellent electric conductivity, high catalytic capability, good flexibility and high surface to volume ratio of the metallic nanoparticles include gold; silver, etc are conformably used as conductive dopants to intensify the electrochemical activities of electrode material [14]. Formation of gold nanoparticles decorated metal-based electrode expands the storage capacity of a metal-based electrode [15]. For example, Tan et al. [14] synthesized AuNPs/nano Co_3O_4 composite via in-situ reduction method. Wang et al. [16] prepared ultrafine Au decorated with onion-like carbon via without using reductant or surfactant. Although Au nanoparticles have been decorated with electrode material, this requires preventing Au nanoparticles with protective nanolayer. Otherside, aggregation befalls against rGO because of their re-stacking effect can limit the electrochemical studies of the graphene. Therefore, the re-staking spacing between the rGO nanosheets expanded with incorporating the gold nanoparticles (AuNPs) in the nanosheets that explore the surface area as well as it allowed building up electrochemical activities of the rGO [17–19]. Yu et al. [20] proposed electrodeposition of the nanocomposites-rGO-AuNPs for high-performance supercapacitor electrode. Chaudhary et al. [21] fabricated ternary Au/ZnO/rGO nanocomposites via a microwave-assisted hydrothermal method. Therefore, a combination of a transition redox metal oxide with a decorating conductive metal AuNPs is an effective

passageway by means of improving the electrical conductivity of the metal oxide that can greatly enhance energy and power performance of the oxide-based electrode.
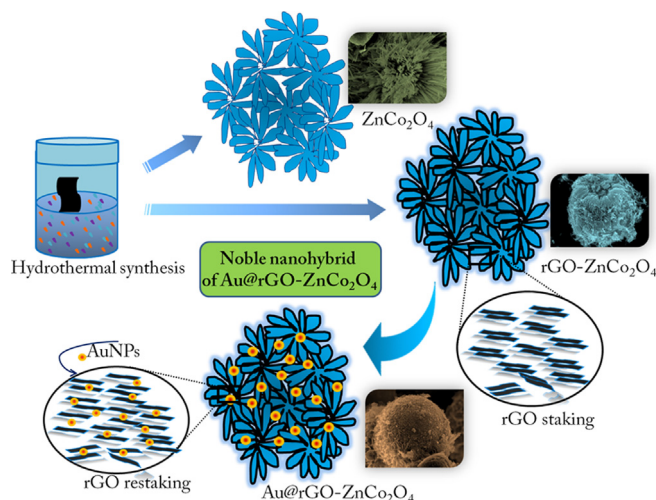
The present work illustrates a new approach to improving supercapacitive performances of the $ZnCo_2O_4$ electrode material. A nanohybrid of well-defined Au@rGO-$ZnCo_2O_4$ is realized for electrochemical studies with concomitant reduction of graphene oxide with decorating AuNPs. This work demonstrates that Au@rGO-$ZnCo_2O_4$ electrode has excellent charge storage capacity performance due to the distribution of AuNPs particles on the surface of rGO-$ZnCo_2O_4$ plays a key role in improving the specific capacity by creating electronic and structural heterogeneity of the electro-active material.

2. Experimental details

Nanostructured Au@rGO-$ZnCo_2O_4$ hybrid was formed using an easy and simple hydrothermal technique. All the chemicals were used without further any purification. In order to prepare rGO-$ZnCo_2O_4$, 10 mg of graphene oxide was added in 45 mL of deionized water (DIW) and ultrasonicated for 1 h to get a sparse suspension. Latterly, 4 mM ammonium fluoride, 1 mM Zinc nitrate, and 2 mM cobalt nitrate were dissolved in the previous solution under constant stirring for 45 min. In the next step, the above solution transferred to Teflon-lined stainless steel autoclave and kept at 150 °C for 12 h. Next, the product was alternately washed with DIW and ethanol and then dried at 60 °C. Subsequently, the obtained samples were annealed at 400 °C for 2 h to remove organic residues that later applied for further studies. Similarly, $ZnCo_2O_4$ was prepared using the same procedure without graphene oxide. In order to incorporate gold nanoparticles, the appropriate amount of prepared rGO-$ZnCo_2O_4$ (0.1 g) was mixed with $HAuCl_4$ (2.0 mg) and sodium citrate (1 wt%, 0.5 mL), and then dissolved in 40 mL DIW under magnetic stirring at 90 °C for 30 min. Further, the solution cooled down to room temperature and washed with DIW and ethanol repeatedly. Finally, the obtained resultant product dried in the oven for overnight and was notified as Au@rGO-$ZnCo_2O_4$ electrode. Scheme 1 illustrates the mechanism of formation of Au@rGO-$ZnCo_2O_4$ cauliflower from the $ZnCo_2O_4$ micro flowers.

2.1. Characterization techniques

Scanning and transmission electron microscopes (FE-SEM and TEM) are a vital characterizations tool were used directly for morphological analysis of the nanostructures and to obtain the quantitative measures of the nanomaterial/particle size. Selected area electron diffraction (SAED) pattern and X-ray diffraction (XRD) were used to identify

Scheme 1. Mechanism of formation of Au@rGO-$ZnCo_2O_4$ cauliflower.

crystal structures and examine crystal defects in the material. X-ray photoelectron spectroscopy (XPS) and energy dispersive X-ray spectroscopy (EDS) is the technique used to find the elemental state and composition ratio of the material. Certain specific surface area was measured according to nitrogen adsorption and desorption isotherms through the Brunauer-Emmett-Teller system (BET) system. The electrochemical performances of $ZnCo_2O_4$ based electrodes were investigated in aqueous KOH solution on an IVIUM Tech electrochemical workstation in a three-electrode cell configuration with a platinum plate and standard calomel electrode (SCE) as the counter and a reference electrode, respectively. The working electrode was prepared by well mixing the Au@rGO-$ZnCo_2O_4$, carbon black and polymer binder (Polytetrafluoroethylene (PTFE)) at a weight ratio of 80:10:10 with few drops of the ethanol. The mixture is well grinded in the agate mortar to form a slurry. Further, the resulting slurry was pasted on the carbon cloth in the unit area and dried at 80 °C in oven for 12 h.

3. Results and discussion

3.1. Micro-structural analysis

Fig. 1(a, b) displays an overview of $ZnCo_2O_4$ nanostructures with uniform micro flower surface morphology. A high-definition micrograph for $ZnCo_2O_4$ shows the aggregation of nanorods to form microflowers with a rod diameter ranging roughly 100 nm and length nearly micron as seen in Fig. 1(b). Reduced graphene oxide (rGO) sheets wrapped $ZnCo_2O_4$ was obtained to improve the porosity of the material [6]. Fig. 1(d, e) illustrate the surface micrographs of the rGO-$ZnCo_2O_4$ material. Influenced by rGO, $ZnCo_2O_4$ was uniformly wrapped with graphene sheets to form a cauliflower-like rGO- $ZnCo_2O_4$. Furthermore, cauliflower rGO-$ZnCo_2O_4$ constrained into impregnation with a $HAuCl_4$ solution, following resultant reduction with $NaBH_4$ that commencing AuNPs fastened in the electrode surface (Fig. 1(g, h)). The rGO-$ZnCo_2O_4$ perceived reduction process, the former microstructure of the rGO-$ZnCo_2O_4$ material expanded smoothly and becomes more porous. Fig. 1(h) displays the surface micrograph with scattered AuNPs over the rGO-$ZnCo_2O_4$ material. The elemental mapping analyses of Au@rGO-$ZnCo_2O_4$ material as shown in Fig. 1 (j), which confirms the uniform distribution of surface elements. At. % compositions of the elements in Au@rGO-$ZnCo_2O_4$ nanohybrid are briefly summarized in Table S1 (Supporting information). EDS analysis and elemental mapping, demonstrating that the Au decorated Zn, Co, and O elements are distributed homogeneously in the materials and exist in a stoichiometric ratio.
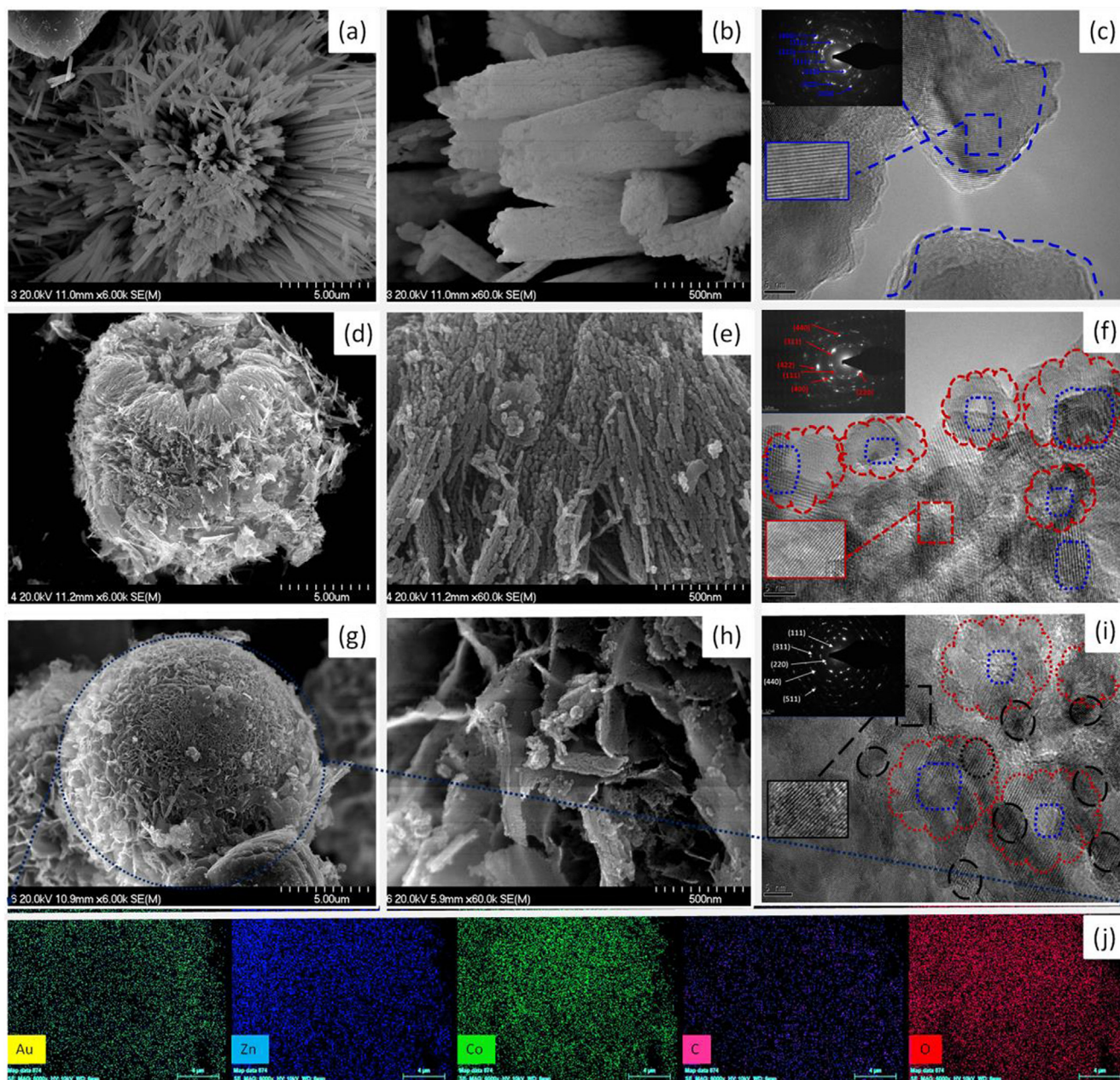
In order to confirm the presence of the Au nanoparticles in the rGO-$ZnCo_2O_4$, HR-TEM analysis is conducted. Fig. 1(c) introduces the clear lattice fringes with an inter-planar spacing of 0.28, 0.24, 0.2, 0.16, and 0.15 nm, which correspond to the (2 2 0), (3 1 1), (4 0 0), (4 2 2) and (2 2 0) planes, respectively, of the cubic spinel $ZnCo_2O_4$ phase. The HR-TEM images of rGO-$ZnCo_2O_4$ revealed that GO was rarely surrounded on the $ZnCo_2O_4$ as shown in Fig. 1(f). The clear lattice fringes with an inter-planar spacing of 0.2, 0.16, 0.15, 0.14 and 0.12 nm which correspond to the (4 0 0), (4 2 2), (2 2 0), (4 4 2) and (5 3 3) planes, respectively, of the cubic spinel rGO-$ZnCo_2O_4$ phase (Fig. 1(f)). Fig. 1(i) reveal the TEM and HR-TEM images of Au@rGO-$ZnCo_2O_4$ material.

The wide range XPS spectra of the $ZnCo_2O_4$ based materials are shown in Fig. 2(a). Fig. 2(b–f) shows the observed XPS spectra of Au@rGO-$ZnCo_2O_4$ confirm the Au nano-particles interconnected in the rGO-$ZnCo_2O_4$ with the presence of C 1s, Zn 2p, Co 2p and O 1s elements in the material without any other impurities. The spectra of Au4f with twosome peaks attributed to the binding energies of 83.2 and 87.3 eV reflecting Au 4f5/2 and Au 4f7/2 as seen in Fig. 2(b), exhibiting the normal oxidation state of Au^0 that approved the formation of AuNPs on rGO-$ZnCo_2O_4$ surface [22]. Au^0 initiate from $NaBH_4$ in parallel to the reduction of Au_x complexes to generate Au^0 nanoparticles from Au^{3+} that is the existence of Au^0 and the species interlocked with the surface

of the rGO-$ZnCo_2O_4$ electrode. As revealed in Fig. 2(c), the peaks at 284.7 eV, 286.0 eV and 288.0 eV are examined by deconvolution of C 1s patterns in accordance with C−C/C=C, C−O, and C=O demonstrating the appearance of effective reduction of GO to rGO in carbon framework [23]. Inset of Fig. 2(c) exhibits spectra of C 1s of $ZnCo_2O_4$ (i) and rGO-$ZnCo_2O_4$ (ii). It shows the intensities of the oxygen-dominated groups (hydroxyl and epoxy groups) were significantly reduced after reduction of graphene oxide. However, a major single peak related to the C−C bond remained predominant, which confirms the structural differences occurred during the reduction process [22]. The main peaks of Zn 2p observed at 1020.6 eV and 1045.4 eV is fitted in a desirable method with two spin-orbit doublets associated to the Zn^{2+} oxidation state (Fig. 2(d)) [24]. The Co 2p emission spectra as seen in Fig. 2(e) was fitted with peaks at 779.2 eV and 794.1 eV of Co^{2+} and Co^{3+} [12]. The characteristics peak at 528.7 eV is of oxygen in the metal oxide, while the other peak at 530.2 eV, 534.2 eV is likely attributed to the structural defects and a hydroxyl group on rGO (as seen in Fig. 2(f)) [25]. Fig. 2(g) displays the XRD pattern of Au@rGO-$ZnCo_2O_4$ material. The peaks detected at 18.9°, 31.46°, 36.95°, 38.48°, 45.05°, 55.57°, 59.59° and 65.18° are indexed as (1 1 1), (2 2 0), (3 1 1), (2 2 2), (4 0 0), (4 2 2), (5 1 1) and (4 4 0) planes of the cubic $ZnCo_2O_4$ structure [26]. The collected XRD data peaks suggest a good match with the conventional diffraction pattern of $ZnCo_2O_4$ (JCPDS card: 00-023-1390) is indicated in the bottom lines. Moreover, the broad peaks were found at the peak positions of 25° and 45° related to reduced graphene oxide. Here no any graphene oxide peak detected in the rGO@$ZnCo_2O_4$ material, suggesting the productive reduction for graphene oxide. In addition, the peaks appear at 38.26°, 44.59°, 64.67°, and 77.54° in Au@rGO-$ZnCo_2O_4$ are corresponds to the Au (JCPDS card: 00-001-1172). Thus, the overall analysis confirms the formation of Au@rGO-$ZnCo_2O_4$. In addition, Raman analysis was further performed to verify the appearance of graphene and Au nanoparticles. Fig. 2(h) shows the Raman spectra of Au@rGO-$ZnCo_2O_4$ sample. Raman spectrum displayed the peaks at 345, 388, 476.1, 860 and 1117 cm^{-1} of $ZnCo_2O_4$ related to the E_g, E_{2g}, and A_{1g}, respectively [27]. While additional two peaks attributed to rGO for the D band arising from sp3 defects/disorder of carbon materials at 1357 cm^{-1} and G band related to the in-plane stretching vibration mode at 1598 cm^{-1} of the graphitized structure of carbon [23]. On the other hand, the Raman bands of rGO and rGO-$ZnCo_2O_4$ sample provided in the supporting information. As compared to GO, the D band are shifted to lower wavenumber (1352 cm^{-1}) in the rGO-$ZnCo_2O_4$ sample by 5 cm^{-1}, whereas the G band (1587 cm^{-1}) showed a blue shift of 12 cm^{-1}. As considering the GO and $ZnCo_2O_4$-rGO spectra, the intensity ratio of the D and G bands (ID/IG) of is 0.96 and 1.25, respectively. It means that the ratio of D and G bands (ID/IG) of the GO is much lower than that of $ZnCo_2O_4$-rGO, which related to the interactions between the $ZnCo_2O_4$ and rGO sheets. This variance implies reducing the strength of sp2 linked carbon atoms due to the elimination of oxygen functional groups in the GO sheet [28].

Nitrogen adsorption-desorption isotherms of the Au@rGO-$ZnCo_2O_4$, material are shown in Fig. 2(i). The surface areas of 37.7 and 47.5 $m^2 g^{-1}$ were determined for $ZnCo_2O_4$ and Au@rGO-$ZnCo_2O_4$ materials, respectively from the adsorption-desorption isotherms. The high BET surface area of Au@rGO-$ZnCo_2O_4$ may also be associated with the effective spacer effect of nanoparticles in between the nanorod covered with nanosheets rGO-$ZnCo_2O_4$. In addition, the corresponding pore volume of the Au@rGO-$ZnCo_2O_4$ electrode materials little increased from 0.32 to 0.51 $cm^3 g^{-1}$. The average pore size of 24 nm for $ZnCo_2O_4$ is reduced to 9.4 nm although incorporating AuNPs that could be ascribed to the re-staking effect and decorated metal nanoparticles within the graphene nanosheets. The large surface area and reliable pore volume of the Au@rGO-$ZnCo_2O_4$ electrode acknowledge successfully interacting with an enormous amount of electrolyte ions in order to realize excellent electrochemical efficiency.
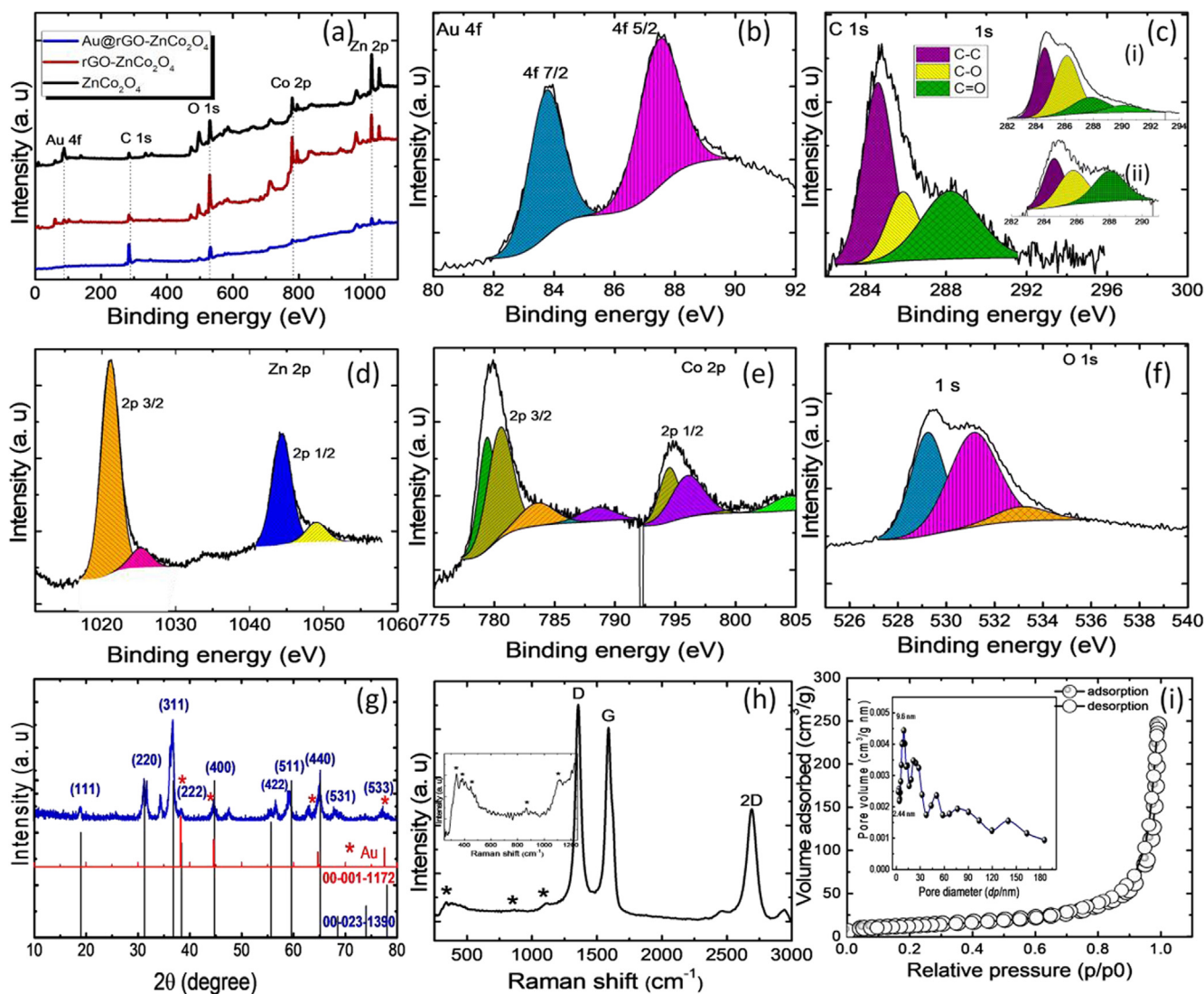
Fig. 1. Scanning electron micrographs of (a, b) $ZnCo_2O_4$, (d, e) rGO-$ZnCo_2O_4$, and (g, h) Au@rGO-$ZnCo_2O_4$ obtained at lower ($\times$6k) and higher ($\times$60 k) magnifications. (c, f and i) are the corresponding highly magnified TEM images and the inset shows the SAED patterns of $ZnCo_2O_4$, rGO-$ZnCo_2O_4$, and Au@rGO-$ZnCo_2O_4$, respectively. (j) Elemental mapping analysis of Au@rGO-$ZnCo_2O_4$, suggesting the presence of Au, Zn, Co, C and O.

4. Electrochemical characterizations

Fig. 3(a) illustrates the comparative cyclic voltammograms (scan rate of $50\,mV\,s^{-1}$) of $ZnCo_2O_4$, rGO-$ZnCo_2O_4$, and the Au@rGO-$ZnCo_2O_4$ electrodes. As expected, Au@rGO-$ZnCo_2O_4$ electrode exhibits a substantially higher current density with the large covered area under the CV curve than that of $ZnCo_2O_4$ and rGO-$ZnCo_2O_4$ electrode can identify a great enhancement in capacitive performance. Fig. 3(b) exhibits CV sweeps at various scanning levels for the Au@rGO-$ZnCo_2O_4$ electrode. The calculated specific capacity with a change in scan rate between 2 and $100\,mV\,s^{-1}$ are outlined in Fig. 3(c) representing datasets concerning $ZnCo_2O_4$, rGO-$ZnCo_2O_4$ and the Au@rGO-$ZnCo_2O_4$ electrodes. At a scan rate of $2\,mV\,s^{-1}$, the storage capacity of the prepared electrodes were evaluated and the Au@rGO-$ZnCo_2O_4$ electrode exhibits a specific capacity of $288.5\,mAh\,g^{-1}$ that is significantly higher than that for $ZnCo_2O_4$ ($193\,mAh\,g^{-1}$) and rGO-$ZnCo_2O_4$

($226.1\,mAh\,g^{-1}$) electrodes. Nevertheless, Au@rGO-$ZnCo_2O_4$ electrode sustains better rate abilities with the scanning rate increase confirming that AuNPs effect on the electrode material. The reduction in specific capacity with scan rate might be due to invalid access of ion electrolyte in the active electrode, which is not sufficient to support the thoroughgoing redox reaction response to the current high rate because of the lower diffusion rate of OH-ions broadcasting into the electrodes [29]. Note that this obtained results is considerably comparable or higher than reported for most $ZnCo_2O_4$ -based electrodes, such as $ZnCo_2O_4$/rGO/sponge electrodes [27], hexagonal $ZnCo_2O_4$ [30], $ZnCo_2O_4$-rGO [31], carbon nanofiber@$ZnCo_2O_4$ [32] etc.

Further, the use of power law is helpfully realizing capacitive-dominated and diffusion-controlled processes to the total charge cover to identify the total difference of processes [33]. The highest dependency scan rate dependent peak current can be expressed as follows (Eq. (1));

Fig. 2. (a) Wideband spectra of $ZnCo_2O_4$, rGO-$ZnCo_2O_4$, and Au@rGO-$ZnCo_2O_4$. The core spectrum of (b) Au 4f, (c) C 1s, (d) Zn 2p, (e) Co 2p, and (f) O 1s of the Au@rGO-$ZnCo_2O_4$. Inset of (c) represents the C1s spectra of the (i) $ZnCo_2O_4$, and (ii) rGO-$ZnCo_2O_4$. (g) XRD, (h) Raman spectrum and (i) Nitrogen adsorption-desorption isotherms of Au@rGO-$ZnCo_2O_4$.
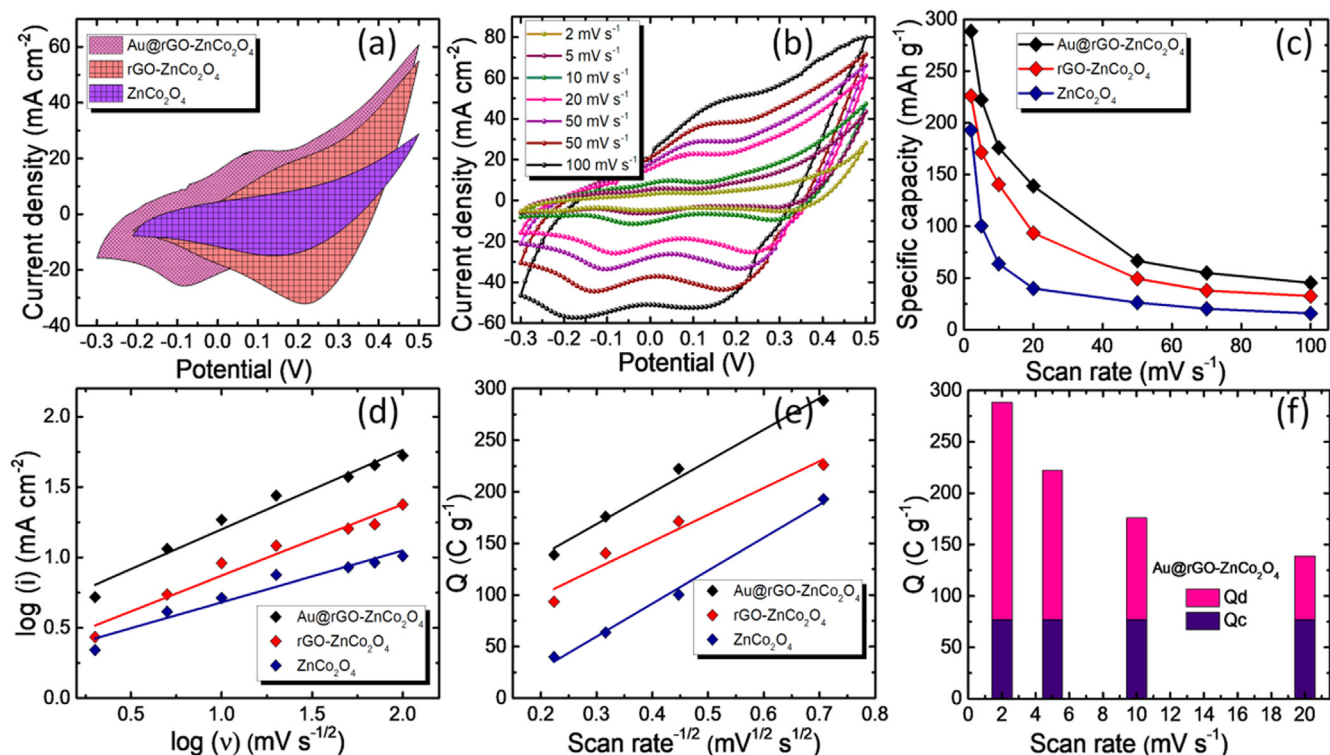
$$ip = av^b \tag{1}$$

where i_p ($mA\,cm^{-2}$), υ ($mV\,s^{-1}$) is a current and scan rate of the CV curves. The adjustable parameters are a and b. In the logarithmic flow and high-quality sensitivity at peak potential, the slope of a line provides b-value and information about the diffusion-controlled or capacitive-dominated processes of the electroactive material with corresponding values in between 0.5 and 1, respectively. Applying the above-mentioned strategy on the CV curves indicates that $ZnCo_2O_4$ based electrode has been kept the highest amount of charge based on the diffusion-controlled method preferably a limited approach of the capacitive-dominated method to low scanning levels. The graphical linear plot of the logarithmic current (i) against logarithmic scan rate (υ) at a peak potential is presented in Fig. 3(d). Further, b-values for the $ZnCo_2O_4$, rGO-$ZnCo_2O_4$ and Au@rGO-$ZnCo_2O_4$ electrodes were evaluated to be 0.36, 0.55 and 0.56, respectively intimating the control of charge storage kinetics processes (i. e diffusion-controlled) [34]. The total charge contribution arises from the capacitive-dominated and diffusion-controlled kinetics occurred at the electrode-electrolyte interface (Fig. 3(e)). However, the capacity of the Au@rGO-$ZnCo_2O_4$ electrode prominently dominated to diffusion-controlled process at a lower scanning rate as displayed in Fig. 3(f).
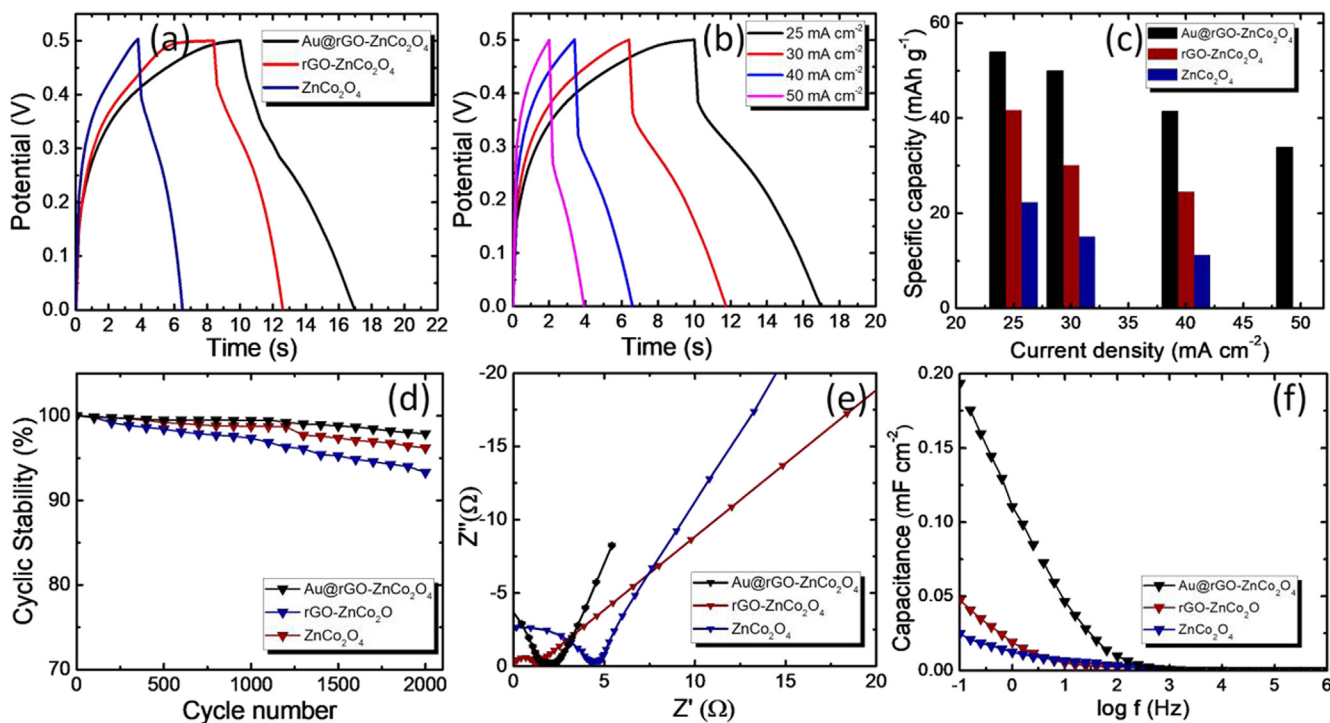
Fig. 4(a) shows galvanostatic charge/discharge profiles conducted at a 25 mA cm^{-2} current density to evaluate the comparative studies for $ZnCo_2O_4$, rGO-$ZnCo_2O_4$ and Au@rGO-$ZnCo_2O_4$ electrodes that maintained a symmetric charge-discharge curve. The nonlinear charge/discharge curve of the Au@rGO-$ZnCo_2O_4$ electrode dissipated in Fig. 4(b) reveals that the contribution of the capacitance from the redox reaction. Indeed, the Au@rGO-$ZnCo_2O_4$ electrode can deliver a higher specific capacity of 54.1 mAh g^{-1} at 25 mA cm^{-2} current density, compared to rGO-$ZnCo_2O_4$ (41.11 mAh g^{-1}) and $ZnCo_2O_4$ (22.22 mAh g^{-1}) electrodes (Fig. 4(c)). High electronic conductivity and good electron affinity of the AuNPs towards the metal oxide, Au@rGO-$ZnCo_2O_4$ electrode shows the great electrochemical performance. In addition, AuNPs plays an amazing role as an electron transfer channels at the discharging time.

Electrochemical cyclic lifespan is one of the highly crucial constituents of the electrochemical energy storage device. The $ZnCo_2O_4$ based electrodes accompanied by cyclic stability of 93, 96 and 97 % for $ZnCo_2O_4$, rGO-$ZnCo_2O_4$ and Au@rGO-$ZnCo_2O_4$ electrodes, respectively over 2000 GCD cycle, as seen in Fig. 4(d). It can be found that capacitance of the electrodes gradually decreased and that its decay observed about 7, 4 and 3% over a continuous 2000 cycles, which shows the long-term stability of Au@rGO-$ZnCo_2O_4$ electrodes. An electronic
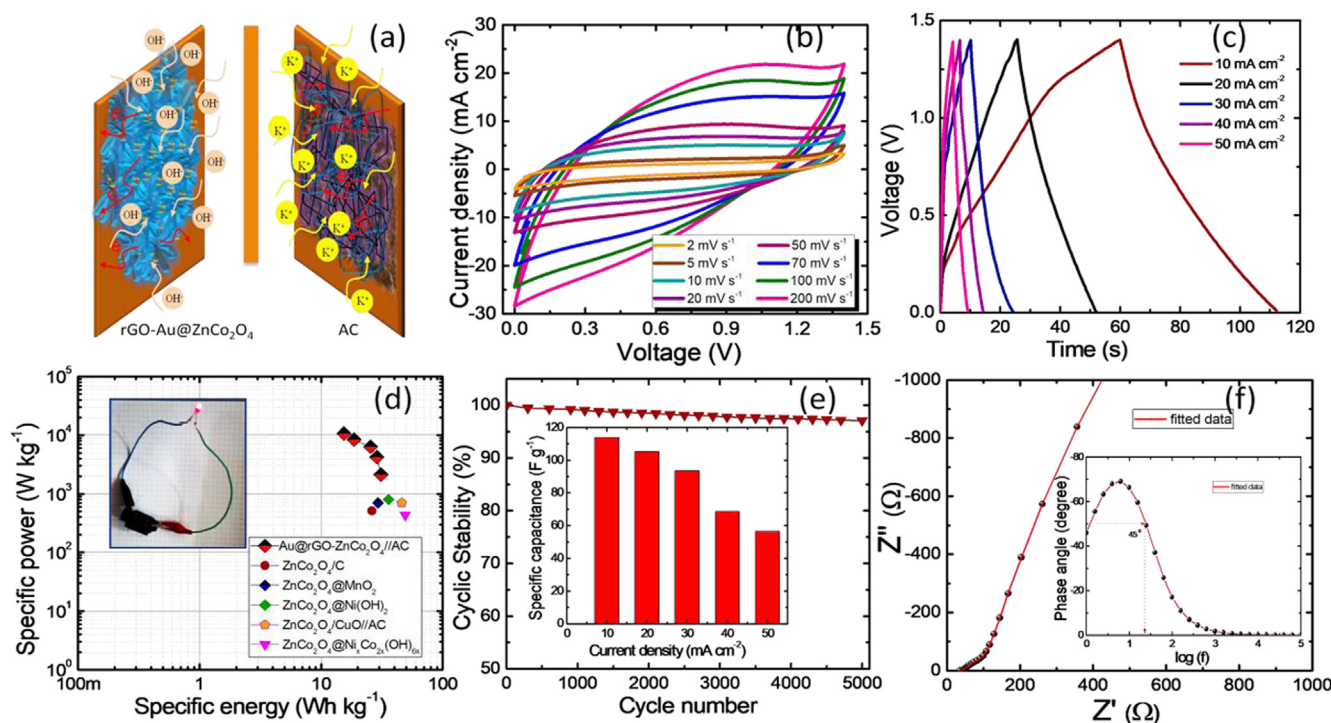
Fig. 3. (a) The comparative CVs of $ZnCo_2O_4$, $rGO\text{-}ZnCo_2O_4$ and $Au@rGO\text{-}ZnCo_2O_4$ electrodes (50 mV s^{-1}). (b) CVs of $Au@rGO\text{-}ZnCo_2O_4$ in KOH electrolyte at various scan rates. (c) The specific capacity plot for the $ZnCo_2O_4$ based electrodes at different scanning rates. (d) Variation of the peak current as a function of scan rate. Estimation of b-values for three electrodes from charge peak currents in corresponding scanning rates. (e) Determinations of slope and intercept values of $ZnCo_2O_4$ based electrodes in different scanning rates. (f) The contribution of capacitive-dominated and diffusion-controlled charge to the total charge stored.

Fig. 4. (a) The comparison of charge/discharge curves and (d) determined the long-term durability of the $ZnCo_2O_4$ based electrodes by measuring charge/discharge (current density of 25 mA cm^{-2}). (b) charge/discharge curves of $Au@rGO\text{-}ZnCo_2O_4$ electrode with different current densities. (c) The column bar presents the specific capacity of the corresponding electrodes calculated from the discharge profiles. (e) The Nyquist plot and (f) normalized capacitance of the $ZnCo_2O_4$ based electrodes of the high and low frequency regions (1 M Hz–0.1 Hz).

Fig. 5. (a) Schematic illustrations for charge storage mechanism of the asymmetric supercapacitor cell fabricated based on Au@rGO-ZnCo$_2$O$_4$ and activated carbon electrodes. (b) The CV and (c) CD profiles of fabricated the hybrid supercapacitor cell with different scanning ranges. (d) The Ragone plot and inset show a photograph of Au@rGO-ZnCo$_2$O$_4$//AC hybrid single cell supercapacitor powered red LED. (e) Cyclic stability performance of the fabricated hybrid single cell supercapacitor evaluated from the charge-discharge profile (inset bar diagram displays the specific capacitance against current density). (f) Impedance analyses of the fabricated hybrid single cell supercapacitor.

conductivity and ion diffusion of ZnCo$_2$O$_4$ based electrodes were interpreted with Nyquist plots. The electrochemical impedance analyses of ZnCo$_2$O$_4$, rGO-ZnCo$_2$O$_4$, and Au@rGO-ZnCo$_2$O$_4$ electrodes further carried out as displayed in Fig. 4(e) conducted for all samples with corresponding a small equivalent series resistance value of 4.3, 1.54 and 1.2 Ω. As can be observed in Nyquist plot (Fig. 4e), the rGO-ZnCo$_2$O$_4$ exhibits slightly greater diffusion resistance than that for bare ZnCo$_2$O$_4$. Owing to the micropores nature of ZnCo$_2$O$_4$, the ion adsorption is confined near the surface zone of microporous, suggesting short ion diffusion lengths. Nevertheless, rGO-ZnCo$_2$O$_4$ exhibits mesopores along with micropores greatly significant for boosting the specific capacity due to the substantial increment in active surface area for ion sorption. In addition, the deep penetration of ions prolongs the diffusion pathway, leading to an increase in ion diffusion resistance of rGO-ZnCo$_2$O$_4$ [35]. The lower resistance value of the Au@rGO-ZnCo$_2$O$_4$ electrode is responsible for the favorable rate capabilities. In addition, Au@rGO-ZnCo$_2$O$_4$ electrode indicates that the short-relaxation time constant (τ0) is 0.17 s obtained with rapid frequency response. The frequency dependent normalized capacitance was calculated from the impedance analysis and results dissipated in Fig. 4(f). In addition, Au@rGO-ZnCo$_2$O$_4$ electrode indicates that the short-relaxation time constant (τ0) is 0.17 s obtained with rapid frequency response.

5. Hybrid supercapacitor device

Schematic illustrations of a fabricated Au@rGO-ZnCo$_2$O$_4$//AC hybrid supercapacitor cell with their CV curves in a three-electrode system (positive (Au@rGO-ZnCo$_2$O$_4$) and a negative electrode (activated carbon)) is dissipated in Fig. S4. Because of Au@rGO-ZnCo$_2$O$_4$ electrode shows the highest specific capacity among different other samples, it was chosen to further examine in the hybrid configuration. To achieve the highest possible voltage by taking advantage of different charge storing mechanism, it is important to balance the stored charges

in both electrodes. To assemble the hybrid cell, the charges stored in two electrodes are balanced with considering their mass loading ratio and it was calculated to be 0.375 by using following equation [12],

$$\frac{m_+}{m_-} = \frac{(C_-\Delta V_-)}{(C_+\Delta V_+)} \tag{2}$$

The weights of Au@rGO-ZnCo$_2$O$_4$ (m_+) and activated carbon electrode materials (m_-) were 0.75 and 2 mg, respectively. C_+ and C_- are the measured specific capacity of positive and negative electrode by CV technique, respectively. To investigate the electrochemical properties of the cell, Au@rGO-ZnCo$_2$O$_4$ and activated carbon (AC) based hybrid cell was assembled using PVA/KOH gel electrolyte. The specific capacity of the Au@rGO-ZnCo$_2$O$_4$ and activated carbon (AC) electrodes optimized to be 48.2 and 18.1 mAh g^{-1}, respectively. Fig. 5(a) presents the schematic illustrations for the charge storage mechanism of the asymmetric supercapacitor cell, where Au@rGO-ZnCo$_2$O$_4$ undergoes reversible faradic reactions with OH$^-$ and K$^+$ ions from the electrolyte were adsorbed/desorbed at the negative electrode (AC) during the charge/discharge process. Fig. 5(b) shows the CV curves of the fabricated flexible cell supercapacitor at different scanning rates varying from 2 to 200 mV s^{-1} in the voltage range from 0 to 1.4 V. Although no visual shape conversion in the CV profile that was apparently by rising the scanning rate confirmed the safely stabilize the tranquility of the seamless interconnection between electrode and electrolyte interfaces with a rapid response to power conversion, which illustrates the effectiveness of the electrochemical device.

The results of the galvanostatic charge/discharge (GCD) tests are consistent with the CV test. The charge/discharge profiles of the fabricated supercapacitor cell are triangular at a higher current density and show good Coulombic efficiency of more than 95%. Aforementioned galvanostatic charge/discharge behavior of the fabricated Au@rGO-ZnCo$_2$O$_4$//AC supercapacitor cell is reflected in the queasy-triangular shape as presented in Fig. 5(c). The specific capacitance of the device

return to be 113.8, 105.2, 93.5, 68.6 and 56.5 F g^{-1} at corresponding current rates of 10, 20, 30, 40 and 50 mA cm^{-2}, respectively. Further, the specific energy and specific power of the fabricated device were calculated from the charge/discharge profiles [25]. Moreover, Au@rGO-ZnCo$_2$O$_4$//AC based hybrid supercapacitor cell (Fig. 5(d)) showed the specific energy density as high as 31 Wh kg^{-1} with a corresponding specific power density of 2.121 kW kg^{-1}. The specific energy and specific power for the assembled supercapacitor have been estimated by considering the active mass of both the electrodes (positive and negative active material). Consequently, the specific energy and power densities of the ZnCo$_2$O$_4$ based hybrid supercapacitor cell were summarized in Ragone plot [36–39].

In order to investigate the practical application, the fabricated hybrid supercapacitor cell demonstrates to power illuminate red light-emitting diode (LEDs) (inset of Fig. 5(d)). The Au@rGO-ZnCo$_2$O$_4$//AC hybrid supercapacitor retained about 97.1% capacity over 5000 cycles (Fig. 5(e)). Impedance analyses of the Au@rGO-ZnCo$_2$O$_4$ supercapacitor cell as dissipated in Fig. 5(f) that was carried out in the frequency range between 10 KHz and 1 Hz. The Nyquist curve for the fabricated supercapacitor cell shows a tilted straight line in 45° to the X-axis in the low to a middle-frequency region. The angle of Au@rGO-ZnCo$_2$O$_4$ based supercapacitor cell accompanying phase frequency (f_0) at −45° is 21 Hz, which reflects the same resistance and capacity barriers. Further, striking the corresponding relaxation time constraint τ_0 (1/f_0) is determined to be 0.047 s represents the fast frequency response towards the electrochemical active sites [40].

6. Conclusions

A ternary nanohybrid of gold nanoparticle decorated rGO-ZnCo$_2$O$_4$ cauliflower was grown on carbon cloth through a facile one-step hydrothermal method followed by a post-annealing treatment. Au@rGO-ZnCo$_2$O$_4$ electrode exhibited high specific capacity with superior cyclic stability due to the porous surface morphology and the corresponding donations of particular ingredients. Further, Au@rGO-ZnCo$_2$O$_4$ electrode based hybrid supercapacitor cell demonstrate an excellent power density of 2.121 kW kg^{-1} and an energy density of 31 Wh kg^{-1} with good capacitive retention (97.01% after 5000 cycles). These results indicate that Au@rGO-ZnCo$_2$O$_4$//AC hybrid supercapacitor cell encourages producing the numerous successful generation of energy storage. In addition, the efficient charge/discharge rates and excellent cyclic stability of the Au@rGO-ZnCo$_2$O$_4$//AC hybrid supercapacitor cell will become more attractive as the energy storage unit for portable devices.

Acknowledgments

Appendix A. Supplementary data

Supplementary data to this article can be found online at https://doi.org/10.1016/j.cej.2019.122211.

References

[1] Y.M. Chiang, Building a better battery, Science 330 (2010) 1485–1486.
[2] D.P. Dubal, O. Ayyad, V. Ruiz, P. Gomez-Romero, Hybrid energy storage: the merging of battery and supercapacitor chemistries, Chem. Soc. Rev. 44 (2015) 1777–1790.
[3] L. Fan, B. Zhu, P.-C. Su, C. He, Nanomaterials and technologies for low temperature solid oxide fuel cells: recent advances, challenges and opportunities, Nano Energy 45 (2018) 148–176.
[4] D.P. Dubal, N.R. Chodankar, D.H. Kim, P. Gomez-Romero, Towards flexible solid-state supercapacitors for smart and wearable electronics, Chem. Soc. Rev. 47 (2018) 2065–2129.
[5] R.S. Sahu, K. Bindumadhavan, R.A. Doong, Boron-doped reduced graphene oxide-based bimetallic Ni/Fe nanohybrids for the rapid dechlorination of trichloroethylene, Environ. Sci. Nano 4 (2017) 565–576.
[6] S.J. Patil, J.H. Kim, D.W. Lee, Graphene-nanosheet wrapped cobalt sulphide as a binder free hybrid electrode for asymmetric solid-state supercapacitor, J. Power Sources 342 (2017) 652–665.
[7] Z. Yang, J. Tian, Z. Yin, C. Cui, W. Qian, F. Wei, Carbon nanotube- and graphene-based nanomaterials and applications in high-voltage supercapacitor: a review, Carbon 141 (2019) 467–480.
[8] C.G. Liu, Z.N. Yu, D. Neff, A. Zhamu, B.Z. Jang, Graphene-based supercapacitor with an ultrahigh energy density, Nano Lett. 10 (2010) 4863–4868.
[9] D.P. Dubal, P. Gomez-Romero, B.R. Sankapal, R. Holze, Nickel cobaltite as an emerging material for supercapacitors: an overview, Nano Energy 11 (2015) 377–399.
[10] C. Wu, J.J. Cai, Q.B. Zhang, X. Zhou, Y. Zhu, L.J. Li, P.K. Shen, K.L. Zhang, Direct growth of urchin-like ZnCo$_2$O$_4$ microspheres assembled from nanowires on nickel foam as high-performance electrodes for supercapacitors, Electrochim. Acta 169 (2015) 202–208.
[11] S. Tajik, D.P. Dubal, P. Gomez-Romero, A. Yadegari, A. Rashidi, B. Nasernejad, Inamuddin, A.M. Asiri, Nanostructured mixed transition metal oxides for high performance asymmetric supercapacitors: Facile synthetic strategy, Int. J. Hydrogen Energy 42 (2017) 12384–12395.
[12] S.J. Patil, D.-W. Lee, Scalable and ascendant synthesis of carbon cloth coated hierarchical core–shell CoMoS@Co(OH)$_2$ for flexible and high-performance supercapacitors, J. Mater. Chem. A 6 (2018) 9592–9603.
[13] N.R. Chodankar, D.P. Dubal, S.H. Ji, D.H. Kim, Superfast electrodeposition of newly developed RuCo$_2$O$_4$ nanobelts over low-cost stainless steel mesh for high-performance aqueous supercapacitor, Adv. Mater. Interfaces 5 (2018) 1800283.
[14] Y. Tan, Y. Liu, L. Kong, L. Kang, F. Ran, Supercapacitor electrode of nano-Co$_3$O$_4$ decorated with gold nanoparticles via in-situ reduction method, J. Power Sources 363 (2017) 1–8.
[15] J. Zhu, Z. Xu, B.N. Lu, Ultrafine Au nanoparticles decorated NiCo$_2$O$_4$ nanotubes as anode material for high-performance supercapacitor and lithium-ion battery applications, Nano Energy 7 (2014) 114–123.
[16] C. Wang, C. Wu, S. Chen, Q. He, D. Liu, X. Zheng, Y.A. Haleem, L. Song, In situ synthesis of noble metal nanoparticles on onion-like carbon with enhanced electrochemical and supercapacitor performance, RSC Adv. 7 (2017) 4667–4670.
[17] P. Wang, Z.-G. Liu, X. Chen, F.-L. Meng, J.-H. Liu, X.-J. Huang, UV irradiation synthesis of an Au–graphene nanocomposite with enhanced electrochemical sensing properties, J. Mater. Chem. A 1 (2013) 9189–9195.
[18] C.L. Scott, M. Pumera, Nanogold spacing of stacked graphene nanofibers for supercapacitors, Electroanalysis 23 (2011) 858–861.
[19] F. Gunes, H.-J. Shin, C. Biswas, G.H. Han, E.S. Kim, S.J. Chae, J.-Y. Choi, Y.H. Lee, Layer-by-layer doping of few-layer graphene film, ACS Nano 4 (2010) 4595–4600.
[20] Z. Yu, S. Sun, M. Huang, Electrodeposition of gold nanoparticles on electrochemically reduced graphene oxide for high performance supercapacitor electrode materials, Int. J. Electrochem. Sci. 11 (2016) 3643–3650.
[21] M. Chaudhary, R. Doong, N. Kumar, T.Y. Tseng, Ternary Au/ZnO/rGO nanocomposites electrodes for high performance electrochemical storage devices, Appl. Surf. Sci. 420 (2017) 118–128.
[22] S.V. Otari, S. Patel, J.-H. Jeong, J.-H. Lee, J.-K. Lee, A green chemistry approach for synthesizing thermostable antimicrobial peptide-coated gold nanoparticles immobilized in an alginate biohydrogel, RSC Adv. 6 (2016) 86808–86816.
[23] X.W. Ma, P. Zhang, Y.Y. Zhao, Y. Liu, J. Li, J.Y. Zhou, X.J. Pan, E.Q. Xie, Role of N doping on the electrochemical performances of ZnCo$_2$O$_4$ quantum dots/reduced graphene oxide composite nanosheets, Chem. Eng. J. 327 (2017) 1000–1010.
[24] H. Chen, G. Jiang, W. Yu, D. Liu, Y. Liu, Q. Huang, Z. Tong, Electrospun carbon nanofibers coated with urchin-like ZnCo$_2$O$_4$ nanosheets as a flexible electrode material, J. Mater. Chem. A 4 (2016) 5958–5964.
[25] D. Yu, Z. Zhang, Y.N. Meng, Y. Teng, Y. Wu, X. Zhang, Q. Sun, W. Tong, X. Zhao, X. Liu, The synthesis of hierarchical ZnCo$_2$O$_4$@MnO$_2$ core–shell nanosheet arrays on Ni foam for high-performance all-solid-state asymmetric supercapacitors, Inorg. Chem. Front. 5 (2018) 597–604.
[26] H. Zhao, Y. Jiang, P. Chen, J. Fu, X. Lu, Z. Hou, CoZn-ZIF-derived ZnCo$_2$O$_4$-framework for the synthesis of alcohols from glycerol, Green Chem. 20 (2018) 4299–4307.
[27] I.K. Moon, S. Yoon, J. Oh, Three-dimensional hierarchically mesoporous ZnCo$_2$O$_4$ nanowires grown on graphene/sponge foam for high-performance, flexible, all-solid-state supercapacitors, Chem. Eur. J. 23 (2017) 597–604.
[28] Q. Ru, Z. Wang, S. Cheng, P. Liu, Xi. Hou, S. Su, F.C.C. Ling, Self assembled rice ball-like ZnCo$_2$O$_4$ inlaid on rGO as flexible anodes with high lithium storage capability and superior cycling stability, Energy Technol. 6 (2018) 1899–1903.
[29] R. Wang, P. Wang, X. Yan, J. Lang, C. Peng, Q. Xue, Promising porous carbon derived from celtuce leaves with outstanding supercapacitance and CO$_2$ capture performance, ACS Appl. Mater. Interfaces 4 (2012) 5800–5806.
[30] V. Venkatachalam, A. Alsalme, A. Alswieleh, R. Jayavel, Double hydroxide mediated synthesis of nanostructured ZnCo$_2$O$_4$ as high performance electrode material for supercapacitor applications, Chem. Eng. J. 321 (2017) 474–484.
[31] Z. Gao, L. Zhang, J. Chang, Z. Wang, D. Wu, F. Xu, Y. Guo, K. Jiang, ZnCo$_2$O$_4$-reduced graphene oxide composite with balanced capacitive performance in asymmetric supercapacitors, Appl. Surf. Sci. 442 (2018) 138–147.
[32] H. Niu, X. Yang, H. Jiang, D. Zhou, X. Li, T. Zhang, J.Y. Liu, Q. Wang, F.Y. Qu,

Hierarchical core–shell heterostructure of porous carbon nanofiber@ZnCo$_2$O$_4$ nanoneedle arrays: advanced binder-free electrodes for all-solid-state supercapacitors, J. Mater. Chem. A 3 (2015) 24082–24094.

[33] P. Sun, W. He, H. Yang, R. Cao, J. Yin, C. Wang, X. Xu, Hedgehog-inspired nanostructures for hydrogel-based all-solid-state hybrid supercapacitors with excellent flexibility and electrochemical performance, Nanoscale 10 (2018) 19004–19013.

[34] R. Giannuzzi, R. Scarfiello, T. Sibillano, C. Nobile, V. Grillo, C. Giannini, P.D. Cozzoli, M. Manca, From capacitance-controlled to diffusion-controlled electrochromism in one-dimensional shape-tailored tungsten oxide nanocrystals, Nano Energy 41 (2017) 634–645.

[35] B.H. Min, K.Y. Jung, Improved porosity and ionic sorption capacity of carbon particles prepared by spray pyrolysis from an aqueous sucrose/NaHCO$_3$/TEOS solution, RSC Adv. 7 (2017) 21314–21322.

[36] W. Fu, Y. Wang, W. Han, Z. Zhang, H. Zha, E. Xie, Construction of hierarchical ZnCo$_2$O$_4$@Ni$_x$Co$_{2x}$(OH)$_{6x}$ core/shell nanowire arrays for high-performance supercapacitors, J. Mater. Chem. A 4 (2016) 173–182.

[37] Y. Pan, H. Gao, M. Zhang, L. Li, G. Wang, X. Shan, Three-dimensional porous ZnCo$_2$O$_4$ sheet array coated with Ni(OH)$_2$ for high-performance asymmetric supercapacitor, J. Colloid Interface Sci. 497 (2017) 50–56.

[38] S. Zhou, Z. Ye, S. Hu, C. Hao, X. Wang, C. Huang, F. Wu, Designed formation of Co$_3$O$_4$/ZnCo$_2$O$_4$/CuO hollow polyhedral nanocages derived from zeolitic imidazolate framework-67 for high-performance supercapacitors, Nanoscale 10 (2018) 15771–15781.

[39] X. Chang, L. Zang, S. Liu, M. Wang, H. Guo, C. Wang, Y. Wang, In situ construction of yolk–shell zinc cobaltite with uniform carbon doping for high performance asymmetric supercapacitors, J. Mater. Chem. A 6 (2018) 9109–9115.

[40] S.J. Patil, J.H. Kim, D.-W. Lee, Self-assembled Ni$_3$S$_2$//CoNi$_2$S$_4$ nanoarrays for ultra high-performance supercapacitor, Chem. Eng. J. 322 (2017) 498–509.